Energy & Environmental Science

ROYAL SOCIETY OF CHEMISTRY

PAPER

View Article Online
View Journal | View Issue

Cite this: *Energy Environ. Sci.*, 2020, **13**, 5048

4 V room-temperature all-solid-state sodium battery enabled by a passivating cathode/hydroborate solid electrolyte interface†

Ryo Asakura, [ab] David Reber, [ac] Léo Duchêne, [ab] Seyedhosein Payandeh, [a] Arndt Remhof, *[a] Hans Hagemann [b] and Corsin Battaglia [a]

Designing solid electrolytes for all-solid-state-batteries that can withstand the extreme electrochemical conditions in contact with an alkali metal anode and a high-voltage cathode is challenging, especially when the battery is cycled beyond 4 V. Here we demonstrate that a hydroborate solid electrolyte $Na_4(CB_{11}H_{12})_2(B_{12}H_{12})$, built from two types of cage-like anions with different oxidative stability, can effectively passivate the interface to a 4 V-class cathode and prevent impedance growth during cycling. We show that $[B_{12}H_{12}]^{2-}$ anions decompose below 4.2 V *vs.* Na^+/Na to form a passivating interphase layer, while $[CB_{11}H_{12}]^-$ anions remain intact, providing sufficient ionic conductivity across the layer. Our interface engineering strategy enables the first demonstration of a 4 V-class hydroborate-based all-solid-state battery combining a sodium metal anode and a cobalt-free $Na_3(VOPO_4)_2F$ cathode without any artificial protective coating. When cycled to 4.15 V *vs.* Na^+/Na, the cells feature a discharge capacity of 104 mA h g^{-1} at C/10 and 99 mA h g^{-1} at C/5, and an excellent capacity and energy retention of 78% and 76%, respectively, after 800 cycles at C/5 at <0.2 MPa at room temperature. Increasing the pressure to 3.2 MPa enables a discharge capacity of 117 mA h g^{-1} at C/10 with a mass loading of 8.0 mg cm^{-2}, corresponding to an areal capacity close to 1.0 mA h cm^{-2}. The cell holds the highest average discharge cell voltage of 3.8 V and specific energy per cathode active material among all-solid-state sodium batteries reported so far, emphasizing the potential of hydroborates as electrolytes for a competitive all-solid-state battery technology.

Received 17th May 2020,
Accepted 1st October 2020

DOI: 10.1039/d0ee01569e

rsc.li/ees

Broader context

All-solid-state batteries are currently one of the most promising options for a next-generation battery technology. They promise improved operational safety and higher energy and power density, compared to state-of-the-art lithium-ion batteries using organic liquid electrolytes. The grand challenge for all-solid-state batteries is the design of a solid electrolyte that meets the requirements in terms of high ionic conductivity and interfacial stability to anode and cathode. Here we employ a hydroborate solid electrolyte that combines liquid-like ionic conductivity, stability against alkali metal anodes, and soft mechanical properties. We show that the self-passivation of the cathode/solid electrolyte interface makes the use of artificial protective layers redundant and enables the stable operation of a 4 V-class all-solid-state battery combining a sodium metal anode and a cobalt-free $Na_3(VOPO_4)_2F$ cathode. Thereby we achieved the highest reported average discharge cell voltage and specific energy per cathode active material among all-solid-state sodium batteries. This work demonstrates the attractive material properties and potential of hydroborate solid electrolytes for a competitive all-solid-state battery technology.

Introduction

Solid electrolytes (SEs) offering high ionic conductivity and high interface stability are key to enable an all-solid-state battery that can compete with today's lithium-ion batteries.[1–5] Several classes of SEs, including oxides, sulfides, halides, and hydroborates, have reached high ionic conductivity of ≥ 1 mS cm^{-1} at room temperature. However, interface stability remains a major challenge.[6,7]

Among oxide SEs, only a few lithium-ion conductors such as $Li_7La_3Zr_2O_{12}$ are highly conductive and sufficiently stable to be

[a] *Materials for Energy Conversion, Empa, Swiss Federal Laboratories for Materials Science and Technology, 8600 Dübendorf, Switzerland. E-mail: arndt.remhof@empa.ch*
[b] *Département de Chimie-Physique, Université de Genève, 1211 Geneva 4, Switzerland*
[c] *Institut des Matériaux, École Polytechnique Fédérale de Lausanne, 1015 Lausanne, Switzerland*

† Electronic supplementary information (ESI) available. See DOI: 10.1039/d0ee01569e

operated with a lithium metal anode.[8–10] For sodium-ion conductors, Na-β″-alumina has shown good compatibility with a sodium metal anode.[11,12] However, the electrochemical oxidative stability of these oxides is limited to ~3.0 V or ~3.8 V against a lithium or sodium metal anode, respectively.[13–15] Sulfide SEs, such as $Li_{10}GeP_2S_{12}$,[16] Li_2S–P_2S_5,[17] Li_6PS_5Cl,[18] or Na_3SbS_4,[19] are not sufficiently stable to be operated in direct contact with a lithium or sodium metal anode and their oxidative stability is only ~2.5 V against the respective alkali metal.[13–15] When cycling 4 V-class cathode active materials in contact with a sulfide SE, a protective cathode coating is typically required to prevent the electrochemical decomposition of the SE into redox active species.[4,20–24] Also, halide SEs such as $Li_{3-x}M_{1-x}Zr_xCl_6$ (M = Y, Er; $0 \leq x \leq 0.6$) or Li_3InCl_6 are recently reported to be compatible with 4 V-class cathodes;[13,25–28] however, due to their instability against lithium metal anodes, protective layers need to be applied on the anode to enable stable battery cycling.[26]

Hydroborates are a yet underexplored class of SEs, but combine very attractive material properties, including compatibility with lithium and sodium metal anodes, low gravimetric density (<1.2 g cm^{-3}), soft mechanical properties enabling cold pressing, high thermal and chemical stability, solution processability, and low toxicity.[29–32] Ionic conductivities ≥ 1 mS cm^{-1} at room temperature are obtained in hydroborate SEs *via* anion mixing of cage-like hydro-*closo*-borate $[B_nH_n]^{2-}$ and/or hydro-*closo*-monocarbaborate $[CB_{n-1}H_n]^-$ ions.[33–39]

So far, stable cycling of all-solid-state lithium and sodium battery cells with metal anodes has been reported for the cell configurations $S|Li(CB_{11}H_{12})_{0.3}(CB_9H_{10})_{0.7}|Li$ and $NaCrO_2|Na_4(B_{12}H_{12})(B_{10}H_{10})|Na$ (or Na–Sn alloy).[37,40,41] In particular, the latter exhibited a cell voltage of ~3 V and an initial discharge capacity of 118 mA h g^{-1} at C/10 with a capacity retention of >95% after 100 cycles at C/5 at 30 °C.[41] Its SE, a 1:1 molar mixture of $Na_2B_{12}H_{12}$ and $Na_2B_{10}H_{10}$, can be synthesized by scalable wet processes from cheap $NaBH_4$ *via* the $[B_3H_8]^-$ intermediate.[42–44] Moreover, intimate contact between the SE and electrode active materials can be obtained by electrolyte solution impregnation of the active material particles[40] or direct infiltration into slurry-casted electrodes.[41]

$Na_4(CB_{11}H_{12})_2(B_{12}H_{12})$ is another hydroborate SE based on a 2:1 molar mixture of $NaCB_{11}H_{12}$ and $Na_2B_{12}H_{12}$. Similarly to $Na_4(B_{12}H_{12})(B_{10}H_{10})$, it was shown to be highly conductive (1–2 mS cm^{-1} at room temperature) and stable against sodium metal.[36,45] As is the case for $Na_2B_{12}H_{12}$, $NaCB_{11}H_{12}$ can also be synthesized from $NaBH_4$ but *via* the $[B_{11}H_{14}]^-$ intermediate,[46–48] allowing cost-effective upscaling of synthesis to industrial volumes. All-solid-state battery cycling with the $Na_4(CB_{11}H_{12})_2(B_{12}H_{12})$ SE was demonstrated so far only using a 3 V-class $NaCrO_2$ cathode in a $NaCrO_2|Na_4(CB_{11}H_{12})_2(B_{12}H_{12})|Na$ cell.[45]

Here we report the first stable room-temperature cycling of a 4 V-class hydroborate-based all-solid-state battery enabled by the *in situ* formation of a passivating interphase layer between the $Na_4(CB_{11}H_{12})_2(B_{12}H_{12})$ SE and a cobalt-free 4 V-class $Na_3(VOPO_4)_2F$ cathode. $Na_3(VOPO_4)_2F$ was chosen as a cathode active material due to its (i) moderate volume change upon cycling (2.2%),[49] (ii) high theoretical capacity (130 mA h g^{-1}), and (iii) stable cycling performance reported in liquid electrolytes.[50–52] In addition, (iv) the redox potentials for the extraction/insertion of two sodium ions per formula unit were adjusted to 3.6 V and 4.0 V *vs.* Na^+/Na by adapting the degree of fluorination of $Na_3(VO_{1-x}PO_4)_2F_{1+2x}$ ($0 \leq x \leq 1$)[49] to maximize the capacity delivered by the cathode active material within the upper voltage cutoff of 4.15 V enabled by the passivation. The resulting high average discharge voltage of 3.8 V and resulting high specific energy per cathode active material mark the highest value among all-solid-state sodium batteries.

In situ passivation of cathode/solid electrolyte interface

Fig. 1 depicts a cross-sectional scanning electron microscopy (SEM) image of the high-voltage all-solid-state battery and its corresponding schematic (see Fig. S1 for the full cross-section, ESI†). The cell comprises a sodium metal anode, a $Na_4(CB_{11}H_{12})_2(B_{12}H_{12})$ SE, and a cathode composite, consisting of $Na_3(VOPO_4)_2F$ as an active material, the SE, and conductive carbon (Super C65) in a 70:20:10 weight ratio. The cathode active material was coated with 5 wt% of the SE by solution impregnation,[40] followed by mixing with 15 wt% of the SE and 10 wt% of carbon in a mortar and subsequent cold pressing. In all-solid-state batteries, since SEs also serve as a separator, no additional separator is needed, unlike lithium-ion batteries using liquid electrolytes.

X-ray diffraction (XRD) patterns and Rietveld refinements of the as-synthesized $Na_4(CB_{11}H_{12})_2(B_{12}H_{12})$ and $Na_3(VOPO_4)_2F$ powders in Fig. S2a and b (ESI†) confirm phase purity based on reported crystal structures.[36,53] Primary $Na_3(VOPO_4)_2F$ particles exhibit plate- and rod-like morphologies with 2–10 μm length and preferred orientation in the [0 0 2] direction (see Fig. S2b and d, ESI†). An elemental map of the cathode composite by energy-dispersive X-ray (EDX) analysis shown in Fig. S3 (ESI†) shows the homogenous distribution of boron. The presence of $Na_3(VOPO_4)_2F$ particles is confirmed by the mapping of vanadium, oxygen, fluorine, and phosphorus, also shown in Fig. S3 (ESI†). $Na_4(CB_{11}H_{12})_2(B_{12}H_{12})$ exhibits thermal stability at least between −20 °C and 180 °C and similar ionic conductivity to that in previous reports (see Fig. S4 and S5, ESI†).[36,45]

Next, we analyze the electrochemical oxidative stability of the mixed-anion $Na_4(CB_{11}H_{12})_2(B_{12}H_{12})$ by cyclic voltammetry

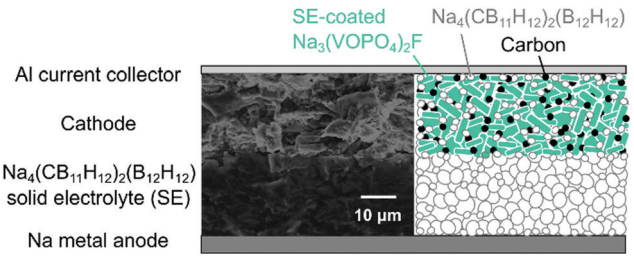

Fig. 1 Cross-sectional SEM image and schematic of 4 V-class $Na_3(VOPO_4)_2F|Na_4(CB_{11}H_{12})_2(B_{12}H_{12})|Na$ all-solid-state cells.

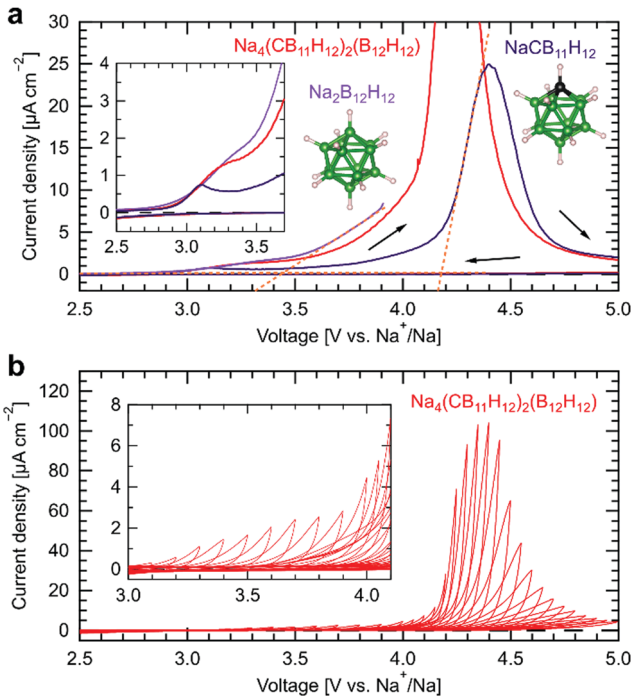

Fig. 2 Electrochemical oxidative stability of hydroborate SEs. (a) Cyclic voltammograms of $Na_2B_{12}H_{12}$ (bright purple), $NaCB_{11}H_{12}$ (dark purple), and $Na_4(CB_{11}H_{12})_2(B_{12}H_{12})$[54] (red) in Na/SE/SE–carbon/Pt cells (SE : carbon = 75 : 25 in weight) at a scan rate of 10 μV s^{-1} at 60 °C. The inset shows the magnified voltammograms. (b) Stepwise voltammograms of $Na_4(CB_{11}H_{12})_2(B_{12}H_{12})$ in the same configuration at a scan rate of 50 μV s^{-1} at 25 °C. The upper cutoff voltage was increased by 0.10 V steps from 2.80 V to 4.00 V *vs.* Na$^+$/Na, followed by 0.05 V steps from 4.00 V to 5.00 V *vs.* Na$^+$/Na. The inset shows the magnified voltammograms.

shown in Fig. 2a, using a SE/carbon composite with a 75 : 25 weight ratio as a working electrode and a platinum disk as a current collector, separated from a sodium metal electrode by a SE without carbon, as previously reported by some of us.[54] To separate the contributions of the two types of anions to the electrochemical oxidation, we also performed cyclic voltammetry of $Na_2B_{12}H_{12}$ and of $NaCB_{11}H_{12}$, individually used as a SE. Measurements are carried out at 60 °C at a low scan rate of 10 μV s^{-1}, because the ionic conductivity of $Na_2B_{12}H_{12}$ and $NaCB_{11}H_{12}$ at room temperature is much lower ($<10^{-5}$ S cm^{-1}) than for the mixed-anion compound $Na_4(CB_{11}H_{12})_2(B_{12}H_{12})$. The onset potentials of electrochemical oxidation of $Na_2B_{12}H_{12}$ and $NaCB_{11}H_{12}$, determined by linear fitting of background and anodic decomposition currents,[54] are 3.45 V and 4.20 V *vs.* Na$^+$/Na, respectively. Decomposition currents below 4 V *vs.* Na$^+$/Na in $Na_4(CB_{11}H_{12})_2(B_{12}H_{12})$ can therefore be attributed to the oxidation of $[B_{12}H_{12}]^{2-}$ ions. Additionally, all three cyclic voltammograms exhibit a minor contribution to the oxidation current with an onset at ~2.9 V *vs.* Na$^+$/Na, which we attribute to solvent residues, as previously observed and discussed for other hydro-*closo*-borates.[54]

To investigate the redox activity of electrochemical decomposition products of $Na_4(CB_{11}H_{12})_2(B_{12}H_{12})$ under cycling conditions, stepwise cyclic voltammetry was conducted in the same cell configuration at 25 °C at a scan rate of 50 μV s^{-1}. The results are shown in Fig. 2b (results at 60 °C for direct comparison with Fig. 2a are shown in Fig. S6b, ESI†). The lower cutoff voltage was fixed at 2.50 V *vs.* Na$^+$/Na, while the upper cutoff voltage was increased by 0.10 V steps from 2.80 V to 4.00 V *vs.* Na$^+$/Na, followed by 0.05 V steps from 4.00 V to 5.00 V *vs.* Na$^+$/Na. As shown in Fig. 2b, anodic currents soar at an upper cutoff voltage of >4.20 V *vs.* Na$^+$/Na, which coincides with the onset potential for $NaCB_{11}H_{12}$ oxidation. It is important to note that there are almost no negative cathodic currents observed during reverse voltage scans in Fig. 2b. Also, anodic currents during the next forward voltage scan remain low up to the upper cutoff voltage of the previous step. This demonstrates (i) that the electrochemical decomposition products of both $[B_{12}H_{12}]^{2-}$ and $[CB_{11}H_{12}]^{-}$ ions are not redox active within the operating voltage range, in contrast to the redox activity of decomposed species in sulfide SEs,[24,55] and (ii) that the decomposition products prevent further oxidation of the electrolyte.

The stability of the $Na_4(CB_{11}H_{12})_2(B_{12}H_{12})$ SE was further studied in contact with the $Na_3(VOPO_4)_2F$ cathode active material in an asymmetric $Na_3(VOPO_4)_2F|Na_4(CB_{11}H_{12})_2(B_{12}H_{12})|Na$ cell by stepwise galvanostatic charge–discharge measurements and electrochemical impedance spectroscopy at 25 °C. As shown in Fig. 3a, the cathode composite was cycled against a sodium metal anode galvanostatically at C/10 (1C = 130 mA g^{-1}, 0.161 mA cm^{-2} for a mass loading of 1.2 mg cm^{-2}) with a fixed lower cutoff voltage of 2.50 V *vs.* Na$^+$/Na. The upper cutoff voltage was increased from 4.05 V to 4.40 V *vs.* Na$^+$/Na in steps of 0.05 V every 5 cycles. Fig. 3b shows the cycle dependence of the discharge capacity and the Coulombic efficiency for increasing upper cutoff voltage. The discharge capacity increases abruptly at 4.10 V *vs.* Na$^+$/Na due to the full utilization of the first and second plateau of $Na_3(VOPO_4)_2F$ at 3.6 V and 4.0 V *vs.* Na$^+$/Na, respectively.[49] The first-cycle Coulombic efficiency is 91.4% at the upper cutoff voltage of 4.05 V *vs.* Na$^+$/Na, followed by >98.5% in the next four cycles. The Coulombic efficiency remains >99% up to an upper cutoff voltage value of 4.25 V *vs.* Na$^+$/Na. At a cutoff voltage of 4.30 V *vs.* Na$^+$/Na, the efficiency starts to drop, coinciding with a gradual decrease in discharge capacity for the rest of the measurements. Furthermore, as shown in Fig. 3a, the higher the upper cutoff voltage, the larger the charge–discharge overpotentials at the two plateaus, and the slopier the charge–discharge curves. This behavior is consistent with the behavior observed in cyclic voltammetry measurements of the SE/carbon composites, corroborating that the electrochemical decomposition products of $[B_{12}H_{12}]^{2-}$ and $[CB_{11}H_{12}]^{-}$ ions in the $Na_4(CB_{11}H_{12})_2(B_{12}H_{12})$ SE are redox inactive. More importantly, these results indicate that the $Na_4(CB_{11}H_{12})_2(B_{12}H_{12})$ decomposition products passivate the cathode/SE interface.

Fig. 3c shows a Nyquist plot of the electrochemical impedance spectroscopy data collected at the initial open-circuit voltage (OCV, 2.4 V *vs.* Na$^+$/Na, denoted as "before cycling") and after a 30 min rest at each upper cutoff voltage during stepwise galvanostatic charge–discharge measurements. At the initial OCV (= "before cycling"), an interfacial contribution is observed as a single semi-circle in the Nyquist representation

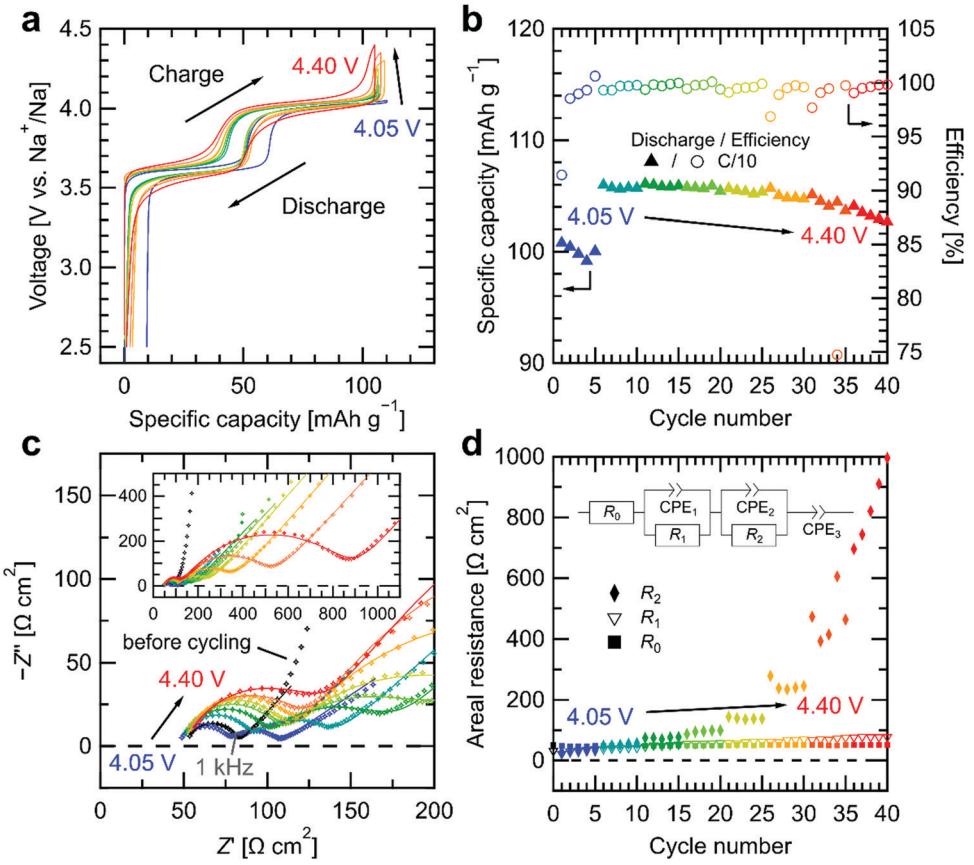

Fig. 3 Formation of a passivating cathode/solid electrolyte interface. (a) Stepwise galvanostatic charge–discharge curves of the first cycle for different upper cutoff voltages and (b) cycling performance of a $Na_3(VOPO_4)_2F|Na_4(CB_{11}H_{12})_2(B_{12}H_{12})|Na$ all-solid-state cell cycled between 2.50 V and 4.40 V *vs.* Na^+/Na at C/10 at 25 °C. The upper cutoff voltage was increased by 0.05 V steps after every 5 cycles from 4.05 V to 4.40 V *vs.* Na^+/Na. (c) Impedance spectra at the initial OCV (denoted as "before cycling") and after a 30 min rest in the second cycle at each upper cutoff voltage. The inset shows the impedance spectra over the full frequency range. (d) Cycle dependence of each resistive contribution of the impedance spectra, fitted with an equivalent circuit shown in the inset. The spectrum at the initial OCV was fitted without the R_2/CPE_2 parallel circuit and is plotted as cycle number 0.

in Fig. 3c at frequencies >1 kHz (see Fig. S7a and b for impedance *vs.* frequency plots, ESI†), along with a resistive contribution at higher frequencies. After galvanostatic cycling at each upper cutoff voltage, an additional interfacial contribution emerges as the second semi-circle in Fig. 3c at low frequencies <1 kHz (see also Fig. S7, ESI†). Both semi-circles expand and shift to lower frequencies with increasing upper cutoff voltage.

Fig. 3d shows the cycle dependence of the different resistive contributions extracted from the Nyquist plots by fitting with an equivalent circuit shown in the inset. Due to the absence of the second semi-circle at the initial OCV, the spectrum was fitted without the parallel R_2/CPE_2 component and is plotted as cycle number 0 in Fig. 3d. The initial contribution R_0 at the highest frequency, representing the left end of the first semi-circle, remains constant at around 50 Ω cm^2 during cycling. R_0 can be attributed to the resistance originating from the $Na_4(CB_{11}H_{12})_2(B_{12}H_{12})$ SE with a conductivity of 1.2 mS cm^{-1}, consistent with reported conductivity values.[36,45] The next contribution R_1 from the first semi-circle in the kHz range increases gradually from 31 Ω cm^2 to 77 Ω cm^2 as cycling proceeds. Nyquist plots of a $Na|Na_4(CB_{11}H_{12})_2(B_{12}H_{12})|Na$ symmetric cell shown in Fig. S8 (ESI†), subjected to galvanostatic cycling with the same capacity per half cycle (0.161 mA h cm^{-2}), shows a single semi-circle with similar behavior. The frequency range of the single semi-circle in Fig. S8 (ESI†) is comparable to that of the first semi-circle in Fig. 3c (see also Fig. S7, ESI†). Moreover, when only one of the two sodium metal/SE interfaces in the symmetric cell is considered, half of the interfacial impedance of the single semi-circle in Fig. S8b (ESI†) gives a similar value (30–50 Ω cm^2) as for R_1 in Fig. 3d. Therefore, we assign R_1 to the sodium metal/SE interface. We attribute the noise on the plateau in Fig. S8a (ESI†) to the high data acquisition rate (every 10 seconds) on this time scale (>500 h). We do not observe either a drastic increase or decrease in overpotential in the symmetric cell, which would be no indication of interphase or dendrite growth, respectively.[12,45]

Inspecting again Fig. 3d, R_2, extracted from the low-frequency semi-circle, first grows with increasing upper cutoff voltage (up to 4.30 V *vs.* Na^+/Na) rather than with the number of cycles. The interfacial impedance remains stable below 80 Ω cm^2 up to 4.15 V *vs.* Na^+/Na, but increases to 100 Ω cm^2

at 4.20 V *vs.* Na^+/Na. At higher cutoff voltages, it grows continuously over cycles up to 1 kΩ cm^2 at 4.40 V *vs.* Na^+/Na, consistent with the stepwise cyclic voltammetry results in Fig. 2b. Since this contribution only appears after cycling with $Na_3(VOPO_4)_2F$, we assign R_2 to the cathode/SE interface, specifically to a passivating resistive interphase forming at the cathode/SE interface. The frequency range of this cathode/SE interphase is consistent with results on sulfide SEs.[20,56,57] These results indicate that the passivating interphase layer formed *via* $[B_{12}H_{12}]^{2-}$ decomposition below 4.20 V *vs.* Na^+/Na still exhibits sufficient ionic conductivity provided by the intact $[CB_{11}H_{12}]^-$ anions and prevents excessive impedance growth. However, above 4.20 V *vs.* Na^+/Na, $[CB_{11}H_{12}]^-$ decomposition sets in, leading ultimately to a more blocking interphase layer.

Loss of contact between SE and $Na_3(VOPO_4)_2F$ particles during cycling cannot be excluded at this point. However, solution impregnation of $Na_3(VOPO_4)_2F$ particles with the hydroborate SEs was shown to offer excellent initial cathode/SE contact in the cathode composite.[40,45] Also, capacity loss during cycling, typically accompanying contact loss, remains minimal as we will show in the following. Furthermore, although $Na_3(VOPO_4)_2F$ contracts by 2.2% upon extraction of two sodium ions by formula unit, additional sodium ion extraction and volume changes only occur at potentials >5 V *vs.* Na^+/Na,[49] which therefore cannot explain a further increase in R_2 above 4.20 V *vs.* Na^+/Na.

In summary, voltammetry and impedance results are consistent with the formation of a passivating, ion-conducting interphase layer at the cathode/SE interface through the irreversible partial decomposition of the less stable $[B_{12}H_{12}]^{2-}$ anion below 4.20 V *vs.* Na^+/Na. At higher voltages, the decomposition of the more stable $[CB_{11}H_{12}]^-$ anion sets in and leads to a blocking interphase layer. The most probable electrochemical oxidation mechanism of the SE is the dimerization of hydro-*closo*-borates and -monocarbaborates.[58,59] The determination of the exact composition and structure of the passivating interphase is very challenging, mainly due to trace amounts forming at the interface hidden by the strong bulk signal, low crystallinity, and minimal change in the oxidation state of the constituent boron atoms in the cage-like anions.[60–62]

Cycling and rate performance of all-solid-state sodium battery cells at room temperature

To assess the long-term cycling stability of the $Na_3(VOPO_4)_2F|Na_4(CB_{11}H_{12})_2(B_{12}H_{12})|Na$ cells, galvanostatic charge–discharge measurements were performed at C/5 (32.2 μA cm^{-2}) following two formation cycles at C/10 at room temperature (see Fig. 4). Based on the previous discussion, the upper cutoff voltage was set to 4.15 V *vs.* Na^+/Na to enable the extraction of two sodium ions per $Na_3(VOPO_4)_2F$ formula unit, while preventing a large increase in cell impedance due to $[CB_{11}H_{12}]^-$ decomposition. For comparison, another cell was cycled up to 4.30 V *vs.* Na^+/Na, which is a typical upper cutoff voltage when cycling $Na_3(VOPO_4)_2F$ in organic liquid electrolytes.[50,51] The Coulombic efficiency of the cell cycled to 4.15 V *vs.* Na^+/Na is only 91.4% in the first cycle and 98.5% in the second cycle, due to the *in situ* formation of the passivation layer at the cathode/SE interface, but improves to >99.8% in later cycles. The cell shows a discharge capacity of 104 mA h g^{-1} at C/10 and excellent cycling performance at C/5 with a reversible capacity of 90 mA h g^{-1} after 400 cycles and 78 mA h g^{-1} after 800 cycles. With respect to the initial discharge capacity of 99 mA h g^{-1} at C/5, this represents an excellent capacity retention of 91% after 400 cycles and 78% after 800 cycles. Furthermore, the charge–discharge curves in Fig. 4b show very small overpotentials at the two plateaus (<30 mV) in the first two cycles and they remain relatively small (~300 mV) after 800 cycles, which results in high energy efficiency (90.6%, 97.3%, and 94.5%, 92.0% in the first, second, 400th, and 800th cycles, respectively) and an excellent energy retention of 89% after 400 cycles and 76% after 800 cycles at C/5. These results demonstrate that the cathode composite maintains intimate contact with the active material *via* a stable cathode/SE interphase formed *in situ* by partial SE decomposition.

The cell with the upper cutoff voltage of 4.30 V *vs.* Na^+/Na exhibits a lower first-cycle Coulombic efficiency and much higher irreversible capacity (81.6% and 17 mA h g^{-1}) than the one with 4.15 V *vs.* Na^+/Na (91.4% and 10 mA h g^{-1}). The charge–discharge curves in the first cycle show an additional capacity gain above 4.15 V *vs.* Na^+/Na. Since the capacity of the second plateau of $Na_3(VOPO_4)_2F$ is already fully extracted below this voltage range, the additional capacity originates from irreversible SE decomposition. The effect of SE decomposition is less prominent during the second cycle with a Coulombic efficiency of 98.3% and later cycles with a Coulombic efficiency of >99.7%. However, it affects long-term cycling performance severely. The discharge capacity decreases gradually down to 43 mA h g^{-1} in the 160th cycle, before rapid cell failure in subsequent cycles. At the 160th cycle, capacity and energy retention reach only 44% and 38%, respectively, along with a substantial increase in overpotentials (>500 mV) at the two plateaus. The cross-sectional SEM image after cycling in Fig. S9 (ESI†) shows no major morphological changes inside the cathode composite and at the cathode/SE interface over cycles, excluding the possibility to attribute the main cause of the capacity fade to contact loss. These confirm the conclusions from impedance spectroscopy in Fig. 3d that cycling above the oxidative stability limit of the more stable $[CB_{11}H_{12}]^-$ anion leads to a blocking interphase layer and emphasizes the importance of understanding the different stages of electrochemical oxidation of the SEs.

To evaluate the rate capability, all-solid-state Swagelok-type cells were cycled galvanostatically from C/10 to 1C at room temperature (see Fig. 5). Note that with such a cell configuration, only a small pressure of <0.2 MPa is applied by a spring. Although the discharge capacity decreases with increasing C-rate, a relatively high capacity of 74 mA h g^{-1} is still obtained at 1C. Moreover, cycling at C/5 during and just after the rate test yields almost the same capacity of 103 mA h g^{-1}. The rate test does not affect the long-term cyclability either, as the cell retains 94% (97 mA h g^{-1}) of its capacity after >150 cycles with high Coulombic efficiency of >99.7%.

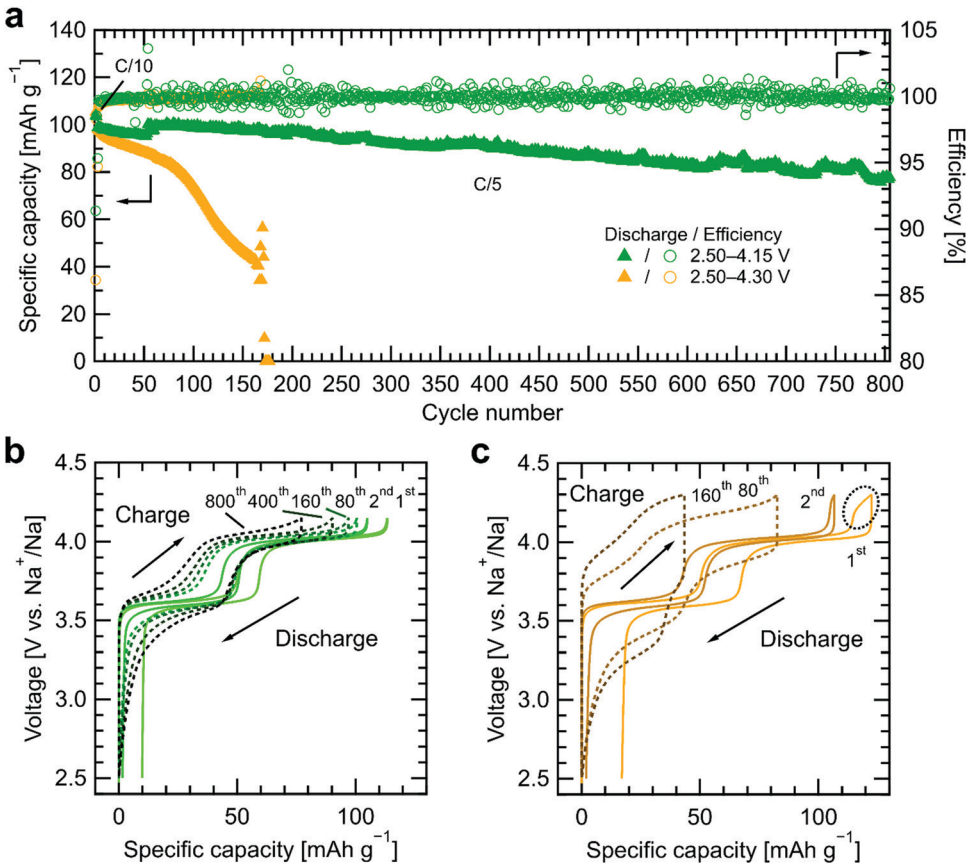

Fig. 4 (a) Long-term cycling performance of $Na_3(VOPO_4)_2F|Na_4(CB_{11}H_{12})_2(B_{12}H_{12})|Na$ all-solid-state cells cycled between 2.50 V and 4.15 V (green) or 4.30 V (yellow) *vs.* Na^+/Na at C/5 following two formation cycles at C/10 at room temperature. Corresponding galvanostatic charge–discharge curves at C/10 (solid) and at C/5 (dashed) with the upper cutoff voltage of (b) 4.15 V and (c) 4.30 V *vs.* Na^+/Na. The dotted circle shows additional capacity derived from irreversible SE decomposition.

This demonstrates that the passivating cathode/SE interphase layer formed during the formation cycling to 4.15 V *vs.* Na^+/Na at C/10 does not hinder cycling at higher C-rates, thereby indicating the possibility of this all-solid-state cell chemistry for high-power applications. At an elevated temperature of 60 °C, the cells show improved rate performance (89 mA h g^{-1} at 1C), but lower capacity retention during long-term cycling at C/5 (see Fig. S10, ESI†). We attribute this to enhanced ionic conductivity of $Na_4(CB_{11}H_{12})_2(B_{12}H_{12})$ and accelerated SE decomposition kinetics, which is in line with voltammetry results in Fig. S6 (ESI†).

Cycling at higher C-rates is enabled by applying an external pressure of 3.2 MPa in a home-built pressure cell. Fig. 5a shows that the pressure cell exhibits a similar discharge capacity up to 1C (0.15 mA cm^{-2} for 1.14 mg cm^{-2} mass loading) compared to the Swagelok-type cell, which applies <0.2 MPa. At even higher rates of 2C (0.30 mA cm^{-2}) and 5C (0.74 mA cm^{-2}), the cell retains capacities of 40 mA h g^{-1} and 11 mA h g^{-1}, respectively, without a short circuit. The added conductive carbon is electrochemically active below 1.50 V *vs.* Na^+/Na.[63] Therefore, we do not expect an effect of the carbon on the capacity within this operating voltage range between 2.50 V and 4.15 V *vs.* Na^+/Na. The pressure cell exhibits excellent cycling performance with a reversible capacity of 96 mA h g^{-1} at C/5 for >150 cycles after the rate test, comparable to Swagelok-type cells. We assign the large capacity drop at higher C-rates to the large particle size (2–10 μm) and long diffusion pathways in $Na_3(VOPO_4)_2F$. Particle size reduction and morphology optimization led to an improvement of rate capability up to 15C in conjunction with organic liquid electrolytes.[50,51] We expect that also in the case of all-solid-state cells, the optimization of the particle size and morphology will further improve the rate capability.

Benefitting from the resilience to high current densities, we cycled a cell with a higher areal capacity close to 1.0 mA h cm^{-2} by increasing the mass loading by a factor of seven to 8.0 mg cm^{-2}, applying again a pressure of 3.2 MPa (see Fig. S11, ESI†). The discharge capacity reaches 90% (117 mA h g^{-1}) of the theoretical capacity of $Na_3(VOPO_4)_2F$ (130 mA h g^{-1}) at C/10 (0.10 mA cm^{-2}) in the first cycle, which is as high as in a liquid-electrolyte reference cell (see Fig. S12, ESI†). The capacity maintains >100 mA h g^{-1} at C/5 (0.21 mA cm^{-2}) for >15 cycles with the Coulombic efficiency of $\geq 99\%$. So far, cells combining a higher cathode mass loading with a sodium metal anode typically fail after <20 cycles due to a short circuit caused by dendrite formation. Extended cycling of sodium metal anodes at such current densities requires suppression of dendrite formation, *e.g.* by further reducing the interfacial

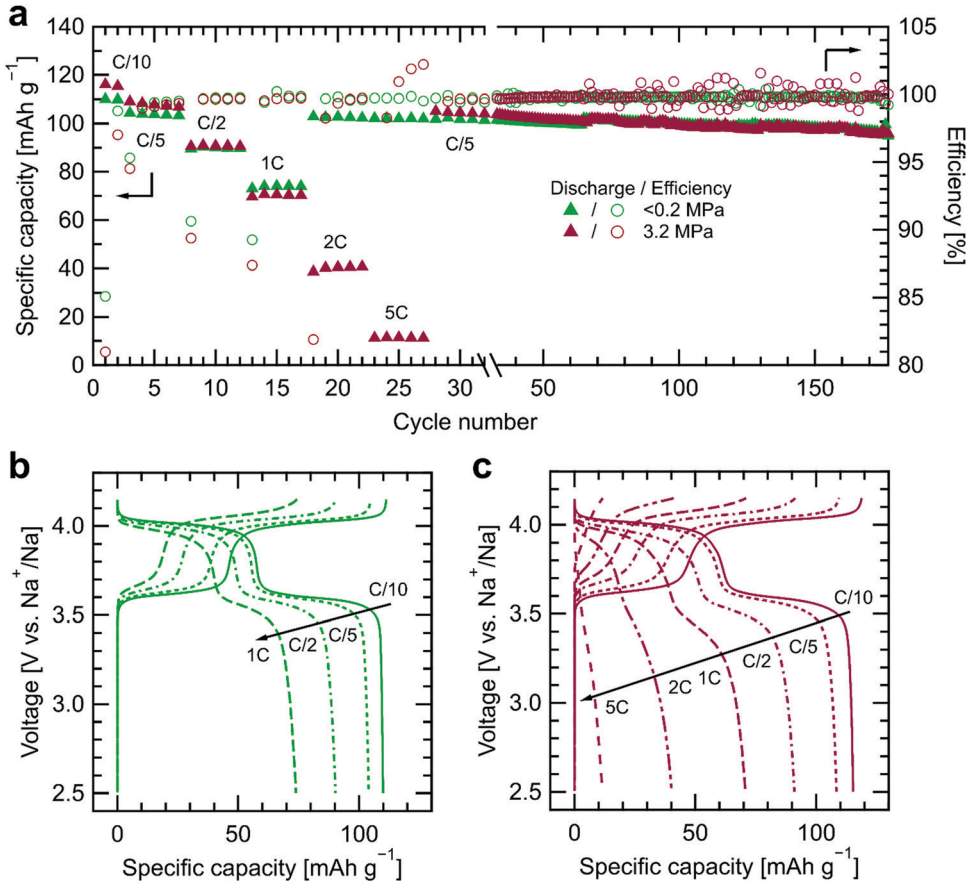

Fig. 5 (a) Rate and cycling performance at different C-rates and during subsequent cycling at C/5 of $Na_3(VOPO_4)_2F|Na_4(CB_{11}H_{12})_2(B_{12}H_{12})|Na$ all-solid-state cells cycled between 2.50 V and 4.15 V *vs.* Na^+/Na at room temperature, without and with external pressure in a Swagelok-type cell (<0.2 MPa) and a home-built pressure cell (3.2 MPa), respectively. Corresponding galvanostatic charge–discharge curves in the second cycle at each C-rate (b) in a Swagelok-type cell (<0.2 MPa) and (c) in a pressure cell (3.2 MPa).

resistance between sodium metal and the SE[9,11] and/or by applying even higher pressure,[8,12,41,64,65] although applying excessive pressure is not desirable for practical applications.[2]

Fig. 6 compares the performance of state-of-the-art all-solid-state sodium and lithium batteries reported in literature, which display >80% capacity retention for ≥100 cycles, using insertion-type cathode active materials. In this figure, specific discharge capacity in mA h $g_{cathode}^{-1}$ is normalized by the cathode composite weight (including the cathode active material, the electrolyte, the conductive carbon, *etc.*). Specific energy in W h $kg_{cathode}^{-1}$ is exhibited as a product of specific discharge capacity and average discharge cell voltage, as recently proposed to enable performance comparison of all-solid-state batteries between different studies and cell chemistries.[2] Each color symbolizes the SEs used: oxides/polymers (blue),[66–69] sulfides (green),[21,23,70–72] and hydroborates (orange and red).[41] All-solid-state cells cycled at elevated temperatures (50–60 °C) are listed with empty symbols with brighter colors (sky blue for oxides/polymers and yellow-green for sulfides), while filled symbols refer to long-term cycling at room temperature or 30 °C. Among all sodium-based cells listed in Fig. 6, the $Na_3(VOPO_4)_2F|Na_4(CB_{11}H_{12})_2(B_{12}H_{12})|Na$ cell in this work shows the highest average discharge cell voltage of 3.8 V comparable to the lithium counterparts, which is enabled by the compatibility of the SE with a sodium metal anode and the *in situ* passivation of the $Na_3(VOPO_4)_2F/Na_4(CB_{11}H_{12})_2(B_{12}H_{12})$ interface without any artificial protective coating. The high average voltage and a reversible capacity reaching 90% of the theoretical capacity of $Na_3(VOPO_4)_2F$ (130 mA h g^{-1}) result in the highest specific energy of 310 W h $kg_{cathode}^{-1}$ with respect to the cathode composite weight among all reported all-solid-state sodium batteries. Note that in principle, the $Na_4(CB_{11}H_{12})_2(B_{12}H_{12})$ SE can be cycled with all listed sodium-based cathode materials, because their operating voltage ranges are within the electrochemical stability window of this hydroborate SE. The deviation of the specific energy from the lithium counterparts is mainly due to the lower specific capacity of the available cathode active materials, as shown in the performance comparison with respect to the cathode active material weight in Fig. S13 (ESI†). To benefit from the advantages of sodium-based batteries, including cobalt-free cathodes, absence of a copper current collector, and the abundance of sodium,[73] new sodium-based cathode active materials combining similarly high redox potentials and higher theoretical capacity compared to $Na_3(VOPO_4)_2F$ are needed for further increase in specific energy to facilitate future applications to electric vehicles and/or stationary energy storage.

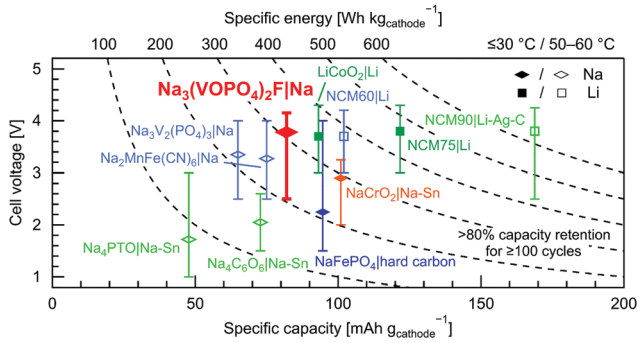

Fig. 6 Comparison of state-of-the-art all-solid-state sodium and lithium battery performance. Specific discharge capacity, average discharge cell voltage, and operating voltage range are plotted for all-solid-state cells exhibiting >80% capacity retention for ≥100 cycles, using insertion-type cathode active materials and SEs based on oxides/polymers (blue),[66–69] sulfides (green),[21,23,70–72] and hydroborates (orange and red).[41] Each specific discharge capacity, normalized by the cathode composite weight in sodiated or lithiated states,[2] was measured at C/10, except for NCM60|Li, NCM75|Li, and $NaFePO_4$|hard carbon at C/5, and for $Na_4PTO|Na–Sn$ at C/7.4 (= C/10 for PTO). Cells cycled at room temperature or 30 °C are listed with filled symbols, while empty symbols with a brighter color (sky blue for oxides/polymers and yellow-green for sulfides) refer to long-term cycling at elevated temperatures (50–60 °C). The abbreviations stand for: PTO = pyrene-4,5,9,10-tetraone, NCM90 = $Li[Ni_{0.90}Co_{0.05}Mn_{0.05}]O_2$, NCM75 = $Li[Ni_{0.751}Co_{0.101}Mn_{0.148}]O_2$, and NCM60 = $Li[Ni_{0.60}Co_{0.20}Mn_{0.20}]O_2$.

Compared to the more heavily investigated oxide- and sulfide-based all-solid-state batteries, hydroborate-based all-solid-state batteries are well on track to reach the research targets recently proposed for all-solid-state batteries (see Table S1, ESI†),[2] including high energy efficiency and retention. To enable higher mass loading and higher areal capacity in the cathode composite and to access higher current density, dendrite formation needs to be suppressed. To reduce the internal cell resistance, the SE thickness and interfacial resistance need to be reduced in the future. These measures will also reduce the weight of the SE used and increase the cell-level specific energy (33 W h kg_{cell}^{-1} in this work) and energy density. The gap in specific energy between all-solid-state sodium batteries and state-of-the-art lithium-ion batteries originates from the available cathode active materials, which is a general issue of sodium-based batteries. Closing the gap requires sodium-based cathode active materials with a similarly high voltage against the respective alkali metal and theoretical capacity to the layered lithium transition metal oxides currently used in lithium-ion batteries.

Conclusions

We demonstrated the first stable room-temperature operation of a 4 V-class hydroborate-based all-solid-state battery. Our interface engineering strategy of combining a less stable anion, responsible for forming a passivating interphase layer, with a more stable anion, to maintain sufficient ionic conductivity across the layer, may be extended to other anion combinations. Integration of even higher-voltage cathode materials remains a future option by extending the oxidative stability limit of the more stable anion *e.g. via* partial halogenation.[74,75] Protective cathode coatings, which have been studied extensively for sulfide-based all-solid-state lithium batteries, remain also an option for future cells.[4,21,23]

Our cells display the highest average discharge cell voltage of 3.8 V and specific energy per cathode active material among all reported all-solid-state sodium batteries, which proves the superior material properties of the hydroborate SE for high-energy batteries. Thus, this works represents a breakthrough not only for hydroborate-based all-solid-state batteries, but also for the future development of a competitive all-solid-state battery technology.

Experimental

Material preparation

$Na_4(CB_{11}H_{12})_2(B_{12}H_{12})$ was prepared by ball milling of $NaCB_{11}H_{12}$ and $Na_2B_{12}H_{12}$ (both KatChem) in a 2 : 1 molar ratio, as reported elsewhere.[36] $Na_2B_{12}H_{12}$ was used as purchased, while $NaCB_{11}H_{12}$ was predried at 250 °C for 12 h under vacuum (10^{-3} mbar).

For electrochemical stability measurements, $Na_2B_{12}H_{12}$ was ball-milled for 3 × 15 min in a 1 : 30 sample-to-ball weight ratio using a Spex 8000M shaker mill, and heat-treated at 300 °C for 12 h under vacuum to enhance its ionic conductivity.[38] $Na_2CB_{11}H_{12}$ was ball-milled likewise without subsequent heat treatment. Conductive carbon Super C65 (Imerys Graphite & Carbon) was dried at 150 °C for 24 h under vacuum.

For the solid-state synthesis of $Na_3(VOPO_4)_2F$,[76] VPO_4 was firstly synthesized by ball milling of stoichiometric amounts of V_2O_5 (>99%, Sigma-Aldrich) and $NH_4H_2PO_4$ (99%, Sigma-Aldrich) in a planetary ball mill (FRITSCH) for 90 min. The mixture was then heat-treated under 95% Ar/5% H_2 at 300 °C for 5 h (at a heating/cooling rate of 0.5 °C min^{-1}), followed by 800 °C for 5 h (3 °C min^{-1}). Secondly, a $VOPO_4$ precursor was synthesized by oxidation of VPO_4 in air at 700 °C for 5 h (3 °C min^{-1}). Thirdly, the stoichiometric amounts of $VOPO_4$, NaF (99.8%, Sigma-Aldrich), and Na_2CO_3 (99.95%, Alfa Aesar) were ball-milled and sintered under argon at 750 °C for 2 h (3 °C min^{-1}). The product was ball-milled in water for 30 min, filtered, and dried at 120 °C overnight in air and for 3 h under vacuum.

All chemicals were stored and handled in an argon-filled glovebox (O_2 and H_2O <0.1 ppm).

Material characterization

X-ray diffraction (XRD) patterns were collected using Cu Kα radiation (λ = 1.54184 Å) in transmission mode with a scan speed of 0.48° min^{-1} using an Empyrean diffractometer and an X'Celerator detector (Malvern Panalytical). Samples were filled in borosilicate glass capillaries under argon atmosphere. Rietveld refinement was carried out with the TOPAS software.[77,78] Scanning electron microscopy (SEM) images were taken at an accelerating voltage of 10 kV using a Nova NanoSEM 230 (FEI). Energy-dispersive X-ray spectroscopy (EDX) elemental maps were acquired at 20 kV using an X-Max Silicon Drift Detector

(Oxford Instruments). Differential scanning calorimetry (DSC) and thermogravimetry (TG) measurements were conducted in an aluminium pan under helium flow at a heating/cooling rate of 5 °C min^{-1} using an STA 449 F3 Jupiter (NETZSCH).

Cell assembly

Three kinds of SE/carbon composites were prepared for electrochemical stability measurements, using $NaCB_{11}H_{12}$, $Na_2B_{12}H_{12}$, and $Na_4(CB_{11}H_{12})_2(B_{12}H_{12})$. Each SE was mixed with Super C65 with a mortar and pestle for 15 min in a 75 : 25 weight ratio, as optimized previously.[54] $Na_3(VOPO_4)_2F$/$Na_4(CB_{11}H_{12})_2(B_{12}H_{12})$/carbon cathode composites in a 70 : 20 : 10 total weight ratio were prepared by solution impregnation.[40] $Na_4(CB_{11}H_{12})_2(B_{12}H_{12})$ was dissolved in anhydrous isopropanol (99.9%, VWR) and $Na_3(VOPO_4)_2F$ was dispersed in the solution by ultrasonication for a few min. The mixture was dried under vacuum and heat-treated at 180 °C for 4 h to obtain SE-coated $Na_3(VOPO_4)_2F$ in a 70 : 5 weight ratio of $Na_3(VOPO_4)_2F$ and $Na_4(CB_{11}H_{12})_2(B_{12}H_{12})$. SE-coated $Na_3(VOPO_4)_2F$ was mixed with the remaining 15 wt% of $Na_4(CB_{11}H_{12})_2(B_{12}H_{12})$ and 10 wt% of Super C65 for 15 min with a mortar and pestle.

For ionic conductivity measurements, 30 mg of $Na_4(CB_{11}H_{12})_2(B_{12}H_{12})$ was pressed uniaxially at 250 MPa into a pellet with quarter inch diameter and 850 μm thickness. Indium foils (≥99.995%, 0.1 mm in thickness, Sigma-Aldrich) with 6 mm diameter were attached on both sides of the pellet to improve contact.[35] For electrochemical stability measurements of SEs, 5 mg of SE/carbon composite and 80 mg of SE were pressed together uniaxially at 150 MPa (for $Na_2B_{12}H_{12}$ and $NaCB_{11}H_{12}$) or 250 MPa (for $Na_4(CB_{11}H_{12})_2(B_{12}H_{12})$) into a 12 mm-diameter pellet. A platinum disk (99.997%, 0.25 mm in thickness, Alfa Aesar) and aluminum foil (>99.3%, 15 μm in thickness, MTI) with 12 mm diameter were attached to the working electrode side of the pellet (= the SE/carbon composite side).[54] A surface-scratched sodium metal foil with 10 mm diameter was rolled out from a sodium metal cube (99.9%, Sigma-Aldrich) and attached on the other side of the pellet as a reference/counter electrode. For the $Na_3(VOPO_4)_2F|Na_4(CB_{11}H_{12})_2(B_{12}H_{12})|Na$ all-solid-state cells, 2 mg of the cathode composite (= 1.2 mg cm^{-2} mass loading) was pre-pressed at 40 MPa and pressed together with 80 mg of $Na_4(CB_{11}H_{12})_2(B_{12}H_{12})$ uniaxially at 250 MPa into a pellet with 12 mm diameter and ~600 μm thickness. An aluminum foil and sodium metal foil were attached to the working and reference/counter electrode sides, respectively. For sodium symmetric cells, 80 mg of $Na_4(CB_{11}H_{12})_2(B_{12}H_{12})$ was pressed at 250 MPa and sodium metal foils were attached on both sides of the pellet. All components were assembled in a two-electrode configuration in a Swagelok-type cell and fixed by a spring with the maximum cell pressure of 0.2 MPa. For measurements with applied external pressure, home-built two-electrode pressure cells were used. In a pressure cell, a 12.5 mm-diameter pellet was formed by cold pressing of 2 mg or 14 mg of the cathode composite (= 1.14 mg cm^{-2} or 8.0 mg cm^{-2} mass loading) and 90 mg of $Na_4(CB_{11}H_{12})_2(B_{12}H_{12})$ at 250 MPa. The pellet was placed between an aluminum foil and sodium metal foil at a constant torque of 0.3 N·m (= 3.2 MPa).

For liquid-electrolyte cells, a slurry consisting of $Na_3(VOPO_4)_2F$, Super C65, and polyvinylidene fluoride (PVDF, Kynar HSV 900, Arkema) in a 90 : 5 : 5 weight ratio, dispersed in an *N*-methyl-2-pyrrolidone (NMP, 99.5%, Sigma-Aldrich) solvent, was casted onto an aluminum foil and pre-dried at 120 °C for 2 h. The electrode sheet was punched out to 12 mm-diameter electrodes, pressed at 170 MPa, and dried at 120 °C for 12 h under vacuum. In a 2032-type coin cell (Hohsen), the electrode and a 12 mm-diameter sodium foil were attached to a 15 mm-diameter Whatman glass fiber separator soaked with 1 M $NaClO_4$ (98%, Alfa Aesar) in propylene carbonate (PC, 99.7%, Sigma-Aldrich): fluoroethylene carbonate (FEC, >99%, Sigma-Aldrich) (98:2 in volume).

Electrochemical characterization

Ionic conductivity was measured between −20 °C and 120 °C under nitrogen flow by electrochemical impedance spectroscopy in a frequency range from 2 MHz to 5 Hz with a 10 mV amplitude using an Alpha-AT impedance analyzer (Novocontrol). All other electrochemical measurements were carried out using a VMP3 or a VSP multichannel potentiostat (BioLogic). For electrochemical stability measurements, cyclic voltammetry was performed between 2.0 V and 6.0 V *vs.* Na^+/Na at a scan rate of 10 μV s^{-1} at 60 °C. Stepwise cyclic voltammetry was conducted between 2.5 V and 5.0 V *vs.* Na^+/Na at a scan rate of 50 μV s^{-1} at 25 °C or 60 °C. The upper cutoff voltage was increased by 0.10 V steps from 2.8 V to 4.0 V *vs.* Na^+/Na, followed by 0.05 V steps from 4.0 V to 5.0 V *vs.* Na^+/Na.

For assessment of the $Na_3(VOPO_4)_2F|Na_4(CB_{11}H_{12})_2(B_{12}H_{12})|Na$ all-solid-state cells, galvanostatic charge–discharge measurements were performed at different C-rates ranging from C/10 to 5C (1C = 130 mA g^{-1}, based on the theoretical capacity of $Na_3(VOPO_4)_2F$) after a 12 h rest at room temperature (25–30 °C) or 60 °C. The lower cutoff voltage was set at 2.50 V *vs.* Na^+/Na, while the upper cutoff voltage was varied by 0.05 V steps at every 5 cycles from 4.05 V to 4.40 V *vs.* Na^+/Na. Likewise, liquid-electrolyte cells were cycled between 2.50 V and 4.30 V *vs.* Na^+/Na at 25 °C. Electrochemical impedance spectroscopy was conducted in a frequency range from 200 kHz to 10 mHz with a 10 mV amplitude at the initial open-circuit voltage (OCV, ~2.4 V *vs.* Na^+/Na) and after a 30 min rest at each upper cutoff voltage. Impedance spectra at each upper cutoff voltage were fitted by an equivalent circuit shown in Fig. 3d ($\chi^2/|Z| < 0.02$). The spectrum at the initial OCV was fitted without the R_2/CPE_2 parallel circuit. In galvanostatic cycling of the $Na|Na_4(CB_{11}H_{12})_2(B_{12}H_{12})|Na$ symmetric cells, a current density of C/5 (32.2 μA cm^{-2} for 1.2 mg cm^{-2} mass loading) was applied for 5 h, corresponding to 0.161 mA h cm^{-2} per half cycle. Between each half cycle, electrochemical impedance spectroscopy was carried out in a frequency range from 500 kHz to 100 mHz with a 10 mV amplitude after a 3 min rest.

Author contributions

R. A., A. R. and C. B. conceived the study and designed the experiments. R. A. conducted the experimental work. D. R. developed

the cathode active material. L. D. developed the home-built pressure cell. S. P. conducted Rietveld refinement. H. H. advised on boron chemistry. R. A., L. D., A. R. and C. B. analyzed the data. R. A., D. R., A. R. and C. B. wrote the manuscript. All authors commented on the manuscript. A. R. and C. B. directed this work.

Conflicts of interest

The authors declare no competing financial interests.

Acknowledgements

This work was partially supported by the Swiss National Science Foundation (SNSF) through under contract 200021L_192191 and InnoSuisse through funding for the Swiss Competence Center for Energy Research (SCCER) Heat and Electricity Storage under contract 1155-002545.

References

1 T. Famprikis, P. Canepa, J. A. Dawson, M. S. Islam and C. Masquelier, *Nat. Mater.*, 2019, **18**, 1278–1291.
2 S. Randau, D. A. Weber, O. Kötz, R. Koerver, P. Braun, A. Weber, E. Ivers-Tiffée, T. Adermann, J. Kulisch, W. G. Zeier, F. H. Richter and J. Janek, *Nat. Energy*, 2020, **5**, 259–270.
3 J. Janek and W. G. Zeier, *Nat. Energy*, 2016, **1**, 16141.
4 Y. Kato, S. Hori, T. Saito, K. Suzuki, M. Hirayama, A. Mitsui, M. Yonemura, H. Iba and R. Kanno, *Nat. Energy*, 2016, **1**, 16030.
5 J. Schnell, T. Günther, T. Knoche, C. Vieider, L. Köhler, A. Just, M. Keller, S. Passerini and G. Reinhart, *J. Power Sources*, 2018, **382**, 160–175.
6 D. H. S. Tan, A. Banerjee, Z. Chen and Y. S. Meng, *Nat. Nanotechnol.*, 2020, **15**, 170–180.
7 Y. Xiao, Y. Wang, S. H. Bo, J. C. Kim, L. J. Miara and G. Ceder, *Nat. Rev. Mater.*, 2020, **5**, 105–126.
8 T. Krauskopf, H. Hartmann, W. G. Zeier and J. Janek, *ACS Appl. Mater. Interfaces*, 2019, **11**, 14463–14477.
9 A. Sharafi, E. Kazyak, A. L. Davis, S. Yu, T. Thompson, D. J. Siegel, N. P. Dasgupta and J. Sakamoto, *Chem. Mater.*, 2017, **29**, 7961–7968.
10 J. Liu, X. Gao, G. O. Hartley, G. J. Rees, C. Gong, F. H. Richter, J. Janek, Y. Xia, A. W. Robertson, L. R. Johnson and P. G. Bruce, *Joule*, 2020, **4**, 101–108.
11 M. Bay, M. Wang, R. Grissa, M. V. F. Heinz, J. Sakamoto and C. Battaglia, *Adv. Energy Mater.*, 2020, **10**, 1902899.
12 D. Spencer Jolly, Z. Ning, J. E. Darnbrough, J. Kasemchainan, G. O. Hartley, P. Adamson, D. E. J. Armstrong, J. Marrow and P. G. Bruce, *ACS Appl. Mater. Interfaces*, 2020, **12**, 678–685.
13 W. D. Richards, L. J. Miara, Y. Wang, J. C. Kim and G. Ceder, *Chem. Mater.*, 2016, **28**, 266–273.
14 Y. Zhu, X. He and Y. Mo, *ACS Appl. Mater. Interfaces*, 2015, **7**, 23685–23693.
15 V. Lacivita, Y. Wang, S. H. Bo and G. Ceder, *J. Mater. Chem. A*, 2019, **7**, 8144–8155.
16 N. Kamaya, K. Homma, Y. Yamakawa, M. Hirayama, R. Kanno, M. Yonemura, T. Kamiyama, Y. Kato, S. Hama, K. Kawamoto and A. Mitsui, *Nat. Mater.*, 2011, **10**, 682–686.
17 F. Mizuno, A. Hayashi, K. Tadanaga and M. Tatsumisago, *Adv. Mater.*, 2005, **17**, 918–921.
18 H. J. Deiseroth, S. T. Kong, H. Eckert, J. Vannahme, C. Reiner, T. Zaiß and M. Schlosser, *Angew. Chem., Int. Ed.*, 2008, **47**, 755–758.
19 A. Banerjee, K. H. Park, J. W. Heo, Y. J. Nam, C. K. Moon, S. M. Oh, S. T. Hong and Y. S. Jung, *Angew. Chem., Int. Ed.*, 2016, **55**, 9634–9638.
20 R. Koerver, I. Aygün, T. Leichtweiß, C. Dietrich, W. Zhang, J. O. Binder, P. Hartmann, W. G. Zeier and J. Janek, *Chem. Mater.*, 2017, **29**, 5574–5582.
21 Y.-G. Lee, S. Fujiki, C. Jung, N. Suzuki, N. Yashiro, R. Omoda, D.-S. Ko, T. Shiratsuchi, T. Sugimoto, S. Ryu, J. H. Ku, T. Watanabe, Y. Park, Y. Aihara, D. Im and I. T. Han, *Nat. Energy*, 2020, **5**, 1–10.
22 A. Y. Kim, F. Strauss, T. Bartsch, J. H. Teo, T. Hatsukade, A. Mazilkin, J. Janek, P. Hartmann and T. Brezesinski, *Chem. Mater.*, 2019, **31**, 9664–9672.
23 Z. Zhang, S. Chen, J. Yang, J. Wang, L. Yao, X. Yao, P. Cui and X. Xu, *ACS Appl. Mater. Interfaces*, 2018, **10**, 2556–2565.
24 G. F. Dewald, S. Ohno, M. A. Kraft, R. Koerver, P. Till, N. M. Vargas-Barbosa, J. Janek and W. G. Zeier, *Chem. Mater.*, 2019, **31**, 8328–8337.
25 X. Li, J. Liang, X. Yang, K. R. Adair, C. Wang, F. Zhao and X. Sun, *Energy Environ. Sci.*, 2020, **13**, 1429–1461.
26 K. H. Park, K. Kaup, A. Assoud, Q. Zhang, X. Wu and L. F. Nazar, *ACS Energy Lett.*, 2020, 533–539.
27 T. Asano, A. Sakai, S. Ouchi, M. Sakaida, A. Miyazaki and S. Hasegawa, *Adv. Mater.*, 2018, **30**(44), 1803075.
28 S. Wang, Q. Bai, A. M. Nolan, Y. Liu, S. Gong, Q. Sun and Y. Mo, *Angew. Chem., Int. Ed.*, 2019, **58**(24), 8039–8043.
29 L. Duchêne, A. Remhof, H. Hagemann and C. Battaglia, *Energy Storage Mater.*, 2020, **25**, 782–794.
30 Z. Lu and F. Ciucci, *Chem. Mater.*, 2017, **29**, 9308–9319.
31 R. Mohtadi and S. Orimo, *Nat. Rev. Mater.*, 2016, **2**, 16091.
32 R. Mohtadi, *Molecules*, 2020, **25**, 1791.
33 T. J. Udovic, M. Matsuo, A. Unemoto, N. Verdal, V. Stavila, A. V. Skripov, J. J. Rush, H. Takamura and S. Orimo, *Chem. Commun.*, 2014, **50**, 3750–3752.
34 W. S. Tang, A. Unemoto, W. Zhou, V. Stavila, M. Matsuo, H. Wu, S. I. Orimo and T. J. Udovic, *Energy Environ. Sci.*, 2015, **8**, 3637–3645.
35 L. Duchêne, R. S. Kühnel, D. Rentsch, A. Remhof, H. Hagemann and C. Battaglia, *Chem. Commun.*, 2017, **53**, 4195–4198.
36 M. Brighi, F. Murgia, Z. Łodziana, P. Schouwink, A. Wołczyk and R. Černý, *J. Power Sources*, 2018, **404**, 7–12.
37 S. Kim, H. Oguchi, N. Toyama, T. Sato, S. Takagi, T. Otomo, D. Arunkumar, N. Kuwata, J. Kawamura and S. Orimo, *Nat. Commun.*, 2019, **10**, 1081.

38 W. S. Tang, M. Matsuo, H. Wu, V. Stavila, A. Unemoto, S. I. Orimo and T. J. Udovic, *Energy Storage Mater.*, 2016, **4**, 79–83.
39 W. S. Tang, K. Yoshida, A. V. Soloninin, R. V. Skoryunov, O. A. Babanova, A. V. Skripov, M. Dimitrievska, V. Stavila, S. I. Orimo and T. J. Udovic, *ACS Energy Lett.*, 2016, **1**, 659–664.
40 L. Duchêne, R. S. Kühnel, E. Stilp, E. Cuervo Reyes, A. Remhof, H. Hagemann and C. Battaglia, *Energy Environ. Sci.*, 2017, **10**, 2609–2615.
41 L. Duchêne, D. H. Kim, Y. B. Song, S. Jun, R. Moury, A. Remhof, H. Hagemann, Y. S. Jung and C. Battaglia, *Energy Storage Mater.*, 2020, **26**, 543–549.
42 A. Gigante, L. Duchêne, R. Moury, M. Pupier, A. Remhof and H. Hagemann, *ChemSusChem*, 2019, **12**, 4832–4837.
43 R. Moury, A. Gigante and H. Hagemann, *Int. J. Hydrogen Energy*, 2017, **42**, 22417–22421.
44 S. Pylypko, S. Ould-Amara, A. Zadick, E. Petit, M. Chatenet, M. Cretin and U. B. Demirci, *Appl. Catal., B*, 2018, **222**, 1–8.
45 F. Murgia, M. Brighi and R. Černý, *Electrochem. Commun.*, 2019, **106**, 106534.
46 S. Payandeh, R. Asakura, P. Avramidou, D. Rentsch, Z. Łodziana, R. Černý, A. Remhof and C. Battaglia, *Chem. Mater.*, 2020, **32**, 1101–1110.
47 J. Pecyna, I. Rončević and J. Michl, *Molecules*, 2019, **24**, 1–13.
48 L. Toom, A. Kütt and I. Leito, *Dalton Trans.*, 2019, **48**, 7499–7502.
49 Y. U. Park, D. H. Seo, H. Kim, J. Kim, S. Lee, B. Kim and K. Kang, *Adv. Funct. Mater.*, 2014, **24**, 4603–4614.
50 Y. Qi, L. Mu, J. Zhao, Y. S. Hu, H. Liu and S. Dai, *Angew. Chem., Int. Ed.*, 2015, **54**, 9911–9916.
51 Y. Qi, Z. Tong, J. Zhao, L. Ma, T. Wu, H. Liu, C. Yang, J. Lu and Y. S. Hu, *Joule*, 2018, **2**, 2348–2363.
52 D. Reber, R.-S. Kühnel and C. Battaglia, *ACS Mater. Lett.*, 2019, **1**, 44–51.
53 N. Sharma, P. Serras, V. Palomares, H. E. A. Brand, J. Alonso, P. Kubiak, M. Luisa Fdez-Gubieda and T. Rojo, *Chem. Mater.*, 2014, **26**, 3391–3402.
54 R. Asakura, L. Duchêne, R. S. Kühnel, A. Remhof, H. Hagemann and C. Battaglia, *ACS Appl. Energy Mater.*, 2019, **2**, 6924–6930.
55 D. H. S. Tan, E. A. Wu, H. Nguyen, Z. Chen, M. A. T. Marple, J. M. Doux, X. Wang, H. Yang, A. Banerjee and Y. S. Meng, *ACS Energy Lett.*, 2019, **4**, 2418–2427.
56 A. Sakuda, A. Hayashi and M. Tatsumisago, *Chem. Mater.*, 2010, **22**, 949–956.
57 W. Zhang, D. A. Weber, H. Weigand, T. Arlt, I. Manke, D. Schröder, R. Koerver, T. Leichtweiss, P. Hartmann, W. G. Zeier and J. Janek, *ACS Appl. Mater. Interfaces*, 2017, **9**, 17835–17845.
58 O. Volkov, C. Hu, U. Kölle and P. Paetzold, *Z. Anorg. Allg. Chem.*, 2005, **631**, 1909–1911.
59 B. T. King, S. Körbe, P. J. Schreiber, J. Clayton, A. Němcová, Z. Havlas, K. Vyakaranam, M. G. Fete, I. Zharov, J. Ceremuga and J. Michl, *J. Am. Chem. Soc.*, 2007, **129**, 12960–12980.
60 Y. Yan, A. Remhof, S. J. Hwang, H. W. Li, P. Mauron, S. I. Orimo and A. Züttel, *Phys. Chem. Chem. Phys.*, 2012, **14**, 6514–6519.
61 M. P. Pitt, M. Paskevicius, D. H. Brown, D. A. Sheppard and C. E. Buckley, *J. Am. Chem. Soc.*, 2013, **135**, 6930–6941.
62 P. Karen, *Angew. Chem., Int. Ed.*, 2015, **54**, 4716–4726.
63 B. Peng, Y. Xu, X. Wang, X. Shi and F. M. Mulder, *Sci. China: Phys., Mech. Astron.*, 2017, **60**, 064611.
64 J. M. Doux, H. Nguyen, D. H. S. Tan, A. Banerjee, X. Wang, E. A. Wu, C. Jo, H. Yang and Y. S. Meng, *Adv. Energy Mater.*, 2020, **10**, 1903253.
65 X. Zhang, Q. J. Wang, K. L. Harrison, S. A. Roberts and S. J. Harris, *Cell Rep. Phys. Sci.*, 2020, **1**, 100012.
66 H. Gao, L. Xue, S. Xin, K. Park and J. B. Goodenough, *Angew. Chem., Int. Ed.*, 2017, **56**, 5541–5545.
67 H. Gao, S. Xin, L. Xue and J. B. Goodenough, *Chem*, 2018, **4**, 833–844.
68 J. K. Kim, Y. J. Lim, H. Kim, G. B. Cho and Y. Kim, *Energy Environ. Sci.*, 2015, **8**, 3589–3596.
69 M. S. Park, Y. C. Jung and D. W. Kim, *Solid State Ionics*, 2018, **315**, 65–70.
70 X. Chi, Y. Liang, F. Hao, Y. Zhang, J. Whiteley, H. Dong, P. Hu, S. Lee and Y. Yao, *Angew. Chem., Int. Ed.*, 2018, **57**, 2630–2634.
71 F. Hao, X. Chi, Y. Liang, Y. Zhang, R. Xu, H. Guo, T. Terlier, H. Dong, K. Zhao, J. Lou and Y. Yao, *Joule*, 2019, **3**, 1–11.
72 S. H. Jung, U. Kim, J. Kim, S. Jun, C. S. Yoon, Y. S. Jung and Y. Sun, *Adv. Energy Mater.*, 2020, **10**, 1903360.
73 C. Vaalma, D. Buchholz, M. Weil and S. Passerini, *Nat. Rev. Mater.*, 2018, **3**, 18013.
74 M. Sharma, D. Sethio, L. M. Lawson Daku and H. Hagemann, *J. Phys. Chem. A*, 2019, **123**, 1807–1813.
75 A. Wahab, C. Douvris, J. Klíma, F. Šembera, J. Ugolotti, J. Kaleta, J. Ludvík and J. Michl, *Inorg. Chem.*, 2017, **56**, 269–276.
76 T. Broux, T. Bamine, F. Fauth, L. Simonelli, W. Olszewski, C. Marini, M. Ménétrier, D. Carlier, C. Masquelier and L. Croguennec, *Chem. Mater.*, 2016, **28**, 7683–7692.
77 A. A. Coelho, J. Evans, I. Evans, A. Kern and S. Parsons, *Powder Diffr.*, 2011, **26**, S22–S25.
78 R. E. Dinnebier, A. Leinweber and J. S. O. Evans, *Rietveld Refinement: Practical Powder Diffraction Pattern Analysis using TOPAS*, De Gruyter, Berlin, 2018.

